



The Precursor Phase of an X-class Flare: Magnetic Reconnection, Powering and Non-thermal Electrons

Jinhua Shen¹, Haisheng Ji^{2,3}, and Yingna Su^{2,3}

¹ Xinjiang Astronomical Observatory, Chinese Academy of Sciences, 150 Science 1-Street, Urumqi, Xinjiang 830011, China; shenjh@xao.ac.cn

² Key Laboratory for Dark Matter and Space Science, Purple Mountain Observatory, CAS, Nanjing, 210023, China; jihs@pmo.ac.cn

³ Purple Mountain Observatory, CAS, Nanjing, 210023, China

Received 2021 August 17; revised 2021 September 26; accepted 2021 October 8; published 2022 January 19

Abstract

In this paper, we report three interesting phenomena that occurred during the precursor phase of the X1.6 class flare on 2014 September 10. (1) The magnetic reconnection initiating the flare occurs between one of the two J-shaped magnetic flux ropes that constitute a sigmoidal structure and the overlying sheared magnetic arcade that runs across the sigmoid over its middle part. The reconnection formed an erupting structure that ultimately leads to flare onset. Another J-shaped magnetic flux rope remains unaffected during the whole eruption. The phenomenon is revealed by the observation made by the Atmospheric Imaging Assembly on board the Solar Dynamic Observatory (SDO) at 94 and 131 Å. (2) Being simultaneously with starting time of the precursor, photospheric vertical electric current (VEC) around the footpoint region of the overlying magnetic arcade underwent an obvious increase, as observed by the Helioseismic and Magnetic Imager (HMI) on board SDO. By only taking into account the VEC with current density over 3σ value ($1\sigma: 10 \text{ mA m}^{-2}$), we are able to pick out precursor-associated VEC increase starting from nearly the level of zero. We regard it as a kind of powering process for the magnetic reconnection between the two magnetic loops. (3) With high-resolution narrow-band Helium 10830 Å images taken by Goode Solar Telescope at Big Bear Solar Observatory (BBSO), we observe a narrow absorption (dark) front that runs along the erupting magnetic structure (or the erupting hot channel) and moves in the direction of the eruption during the precursor phase. Assuming the excitation mechanism of Helium atoms along the absorption front by non-thermal electrons, the phenomenon shows that the interaction between the erupted hot channel and the overlying (or surrounding) magnetic field has yielded electron acceleration.

Key words: magnetic reconnection – Sun: flares – Sun: magnetic fields

Online material: animation

1. Introduction

Solar eruptions are the result of sudden release of free magnetic energy stored in the corona. Magnetic reconnection is believed to play a key role in triggering various solar eruptions of different scales, such as flares, coronal mass ejections (CMEs) and jet events (Priest & Forbes 2000; Schrijver 2009; Fletcher et al. 2011). However, limited by telescopes temporal and spatial resolution, where and how the triggering process of magnetic reconnection occurs in the source region of solar eruptions are still not very clear. In recently years, more and more evidence has been reported giving that flares are triggered during their precursor phases (Tappin 1991; Patsourakos et al. 2013; Bamba et al. 2017; James et al. 2017). The term precursor was proceeded by its old version "preflares" as named by Bumba & Křivský (1959) describing the phenomenon of transient brightenings before the main impulsive phase of a flare. During precursor phase of a flare, small well-pulsed peaks across the electromagnetic spectrum from radio to X-rays appear before the flare

onset (Chifor et al. 2007) and references therein. Soft X-ray (SXR) flux usually starts to rise slowly, with some peaks, before the impulsive of a flare, and the peaks are defined as the flare's X-ray precursors (Harrison et al. 1985; Tappin 1991; Bamba et al. 2017). Flare precursors in microwave and X-ray emissions have been extensively studied via the fine spectral structures and images (Warren & Warshall 2001; Fárník et al. 2003; Kashapova et al. 2012; Zhang et al. 2015; Chen et al. 2019; Hernandez-Perez et al. 2019). A variety of phenomena from multi-wavelength observations have been reported for precursors, which include quasi-periodic oscillations (Fárník et al. 2003; Tan et al. 2016; Zhou et al. 2016; Li et al. 2018); pre-flare coronal dimming (Zhang et al. 2017); the newly emerging flux and canceling near the polarity inversion line (PIL) (Chifor et al. 2006, 2007; Sterling et al. 2010); pre-eruption brightenings in H_{α} /EUV images (Wang et al. 2017; Awasthi et al. 2018); and magnetic flux ropes (MFRs) as hot channels (see below) (Zhang et al. 2012; Cheng et al. 2014). In addition, the presence of non-thermal electrons shown in hard X-ray/microwave emissions and

spectral lines during precursor phases has been widely reported (Fárník et al. 2003; Holman et al. 2003; Asai et al. 2006; Kashapova et al. 2012). Recently, Chen et al. (2019) reported that non-thermal emissions at 3.9–7.9 GHz were observed at conjugate flux rope footpoints during the initiation phase of a flare.

For magnetic configuration before a flare, Moore et al. (1987) proposed a kind of internal sheared core field, often mentioned as sigmoidal flux ropes, being inside a potential external envelope. The sheared core field consists of two groups of highly sheared J-shaped arches rooted close to the PIL crossing the middle of a bipolar magnetic field. With a mechanism known as tether-cutting, Moore et al. (2001) further proposed that magnetic reconnection between the adjoining parts of the J-shaped arches can occur allowing the newly formed MFR, unleashed part of the core field, to expand upward. The sigmoidal flux ropes were originally observed in SXRs (Rust & Kumar 1996; Aurass et al. 1999; Canfield et al. 1999), and they become frequently observed in the AIA’s two hottest coronal passbands at 94 Å (6.4 MK) and 131 Å (10 MK), known as hot channels (Cheng et al. 2011; Zhang et al. 2012). The hot channels often appears sigmoidal structures prior to solar flares/CMEs eruption, which is believed to be the progenitor of CME flux ropes in the lower corona (Cheng et al. 2011; Zhang et al. 2012; Patsourakos et al. 2013). The relationship between precursors and hot channels was also revealed by Patsourakos et al. (2013). During pre-flare phase, an X-ray precursor can be the result of magnetic reconnection between two hot channels, forming a continuous expanding hot channel for a flare’s onset (Shen et al. 2017). Wang et al. (2018) further revealed that the eruption of two hot channels produced two emission peaks in a flare. The two hot channels, including the one that failed to erupt, were produced with magnetic reconnections during the flare’s precursor phase. These results further support that magnetic reconnection between hot channels is the triggering mechanism of eruption of flares/CMEs, remaining questions are how the magnetic reconnection occurs and how it is powered.

For the X1.6-class flare on 2014 September 10 (SOL2017-09-10T17:20), Cheng et al. (2015) reported the formation of a sigmoid MFR by the tether-cutting reconnection in the lower atmosphere. A prototype of sigmoid MFR had its repetitive appearance and disappearance before onset of flare. Finally, a well-shaped sigmoid flux rope was fully formed at 16:55 UT (see Figure 3 of Cheng et al. 2015). In this paper, we will try to explore how the reconnection occurred and what powered the reconnection. The event has also been extensively studied by several other authors (Graham & Cauzzi 2015; Li & Zhang 2015; Li et al. 2015; Tian et al. 2015; Dudík et al. 2016; Zhao et al. 2016). For its precursor phase, oscillations of an MFR and pre-flare coronal dimming have been reported by Zhou et al. (2016) and Zhang et al. (2017). The event was well

observed by the 1.6 m aperture Goode Solar Telescope at Big Bear Solar Observatory (GST/BBSO) with high-resolution narrow-band imaging at He I 10830 Å and broad-band imaging at TiO 7057 Å. It motivates us to find some helpful signatures in the lower atmosphere including the variation magnetic field during the precursor phase. We give a brief description of observations in Section 2. Main results are presented in Section 3. In Section 4, we give a short discussion and summarize the results of the paper.

2. Observations

On 2014 September 10, there were two flare-prolific active regions on solar disk, NOAA 12157 and 12158. Both are $\beta\alpha\sigma$ type according to Hale classification. We selected to observe NOAA 12158, using the 1.6 m aperture GST at BBSO (Cao et al. 2010; Goode et al. 2010). GST’s field of view was further selected to target the satellite sunspot that lies on east of the active region, where a filament was rooted. Meanwhile, IRIS satellite was coordinated to observe the same region. The coordinated observations between BBSO and IRIS on the day were carried out in order to study the precursor process of a possible flare. High spatial resolution images were obtained through the broadband filter (10 Å) containing the TiO 7057 Å line with pixel size of 0''.034, as well as a narrowband 10830 Å (0.5 Å) Lyot filter. The narrowband filter was turned to -0.25 Å from the line center, which was aimed to trace the upward motion of the chromosphere material in the background of the photosphere. The resolution for He I 10830 Å images is 0''.079 per pixel. The GST’s field of view is about 85'' and the imaging cadence is up to 15 s via the high order adaptive optics and the speckle reconstruction (Wöger & von der Lühe 2007). The observation turned out to be very successful, the X1.6-class flare on 2014 September 10 was well observed including its precursor period.

We also use space observations made by Atmospheric Imaging Assembly (AIA) (Lemen et al. 2012) and Helioseismic and Magnetic Imager (HMI) (Scherrer et al. 2012) on board Solar Dynamics Observatory (SDO) (Pesnell et al. 2012). For this event, we use the AIA 94 Å (Fe XVIII; $\log T = 6.8$) as well as 131 Å (Fe XX ; $\log T = 7.1$) to trace the behaviors of hot channels in the precursor phase. In addition, 171 Å (Fe IX; $\log T = 5.8$) images are used to show the surrounding cool context of EUV hot channels. The cadence of AIA images at extreme ultraviolet (EUV) is 12 s, with the spatial resolution 1''.2. HMI observe the vector magnetograms in the Fe I absorption line at 6173 Å with a temporal cadence of 12 minutes and a spatial resolution of 1''. For this paper, we use the data series hmi.sharp-720 s from HMI pipeline (Sun 2013). The vector magnetic field was transformed into the heliographic coordinates, and the 180 degree ambiguity of the transverse field is resolved the minimum energy method (Metcalf et al. 1994).

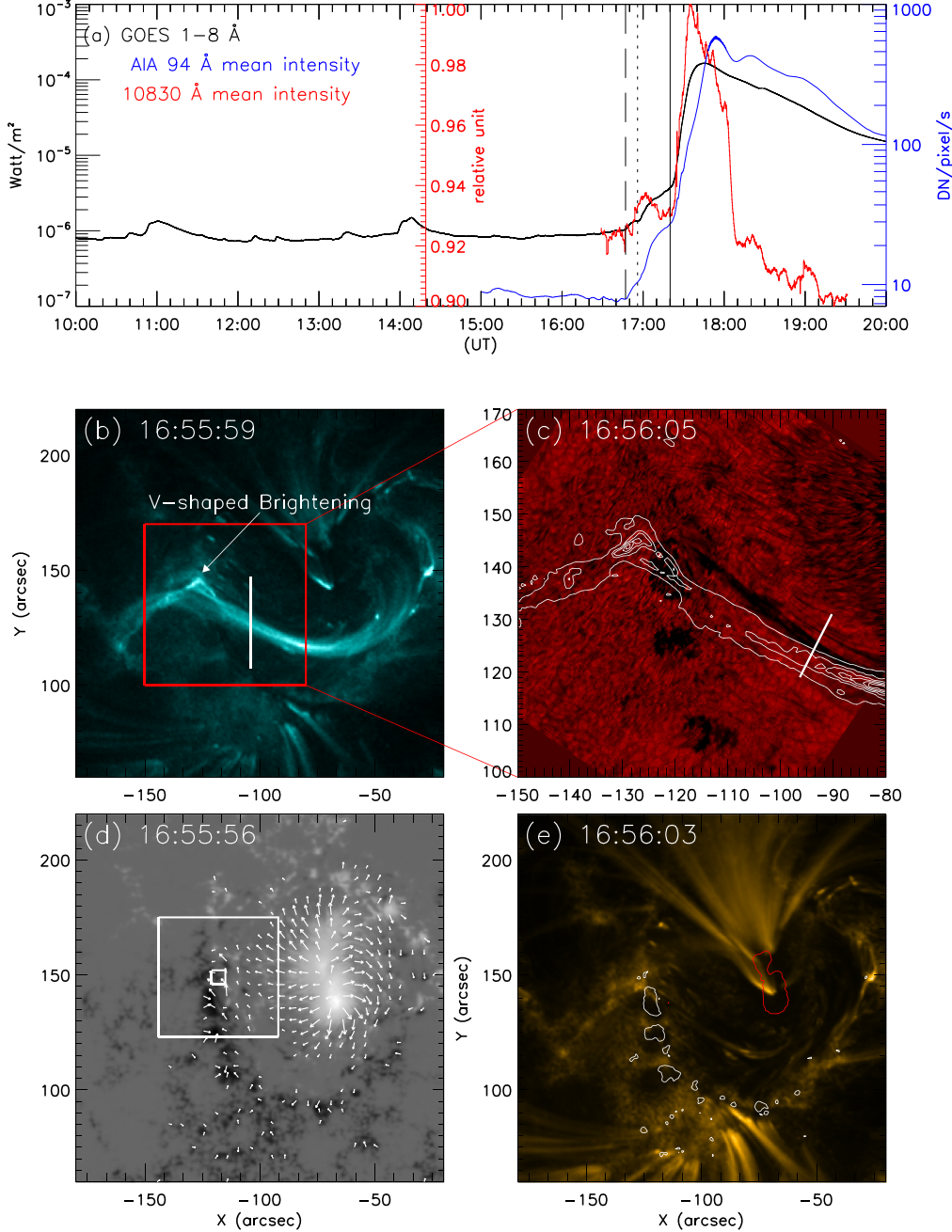


Figure 1. Basic temporal, spatial and multi-wavelength information for the flare. Upper panel (a) gives its time profiles in 1–8 Å (black), 94 Å (blue) and 10830 Å (red) integrated over full disk or the entire flare region. The dashed and solid lines indicate the starting times of the precursor phase (\sim 16:46 UT) and onset moment of the flare (\sim 17:20 UT), while the dotted line indicates the time for the lower four panels. Panels (b) and (c) give an SDO/AIA 131 Å (\sim 10–16 MK) image and a corresponding GST Helium I 10830 Å image, showing the formation of the unstable hot channel and the associated filament. The arrow in panel (b) points to the V-shaped brightening mentioned in the paper. On the 10830 Å image, contours of the hot channel are over-plotted and its FOV ($70'' \times 70''$) corresponds to the red box in the left panel. Panels (d) and (e) give a vector magnetogram and an AIA 171 Å (\sim 0.5–1 MK) image, which is overlaid with contours of LOS magnetic field with the values of 2000 (red) and -1000 G (white). On the vector magnetogram, arrows show horizontal magnetic fields and only those larger than 200 G are plotted. The arrows' lengths scale the magnitude of the horizontal magnetic fields. The two white boxes in panel (d) are the areas for following study of magnetic properties. The two white lines cut two slits for making the spacetime diagram in Figure 2. An online animation of Figure 1 is available.

(An animation of this figure is available.)

3. Results

The X-1.6 class flare occurred on 2014 September 10 in the active region NOAA 12158, where magnetic structure formed a large inverse-sigmoidal structure prior to the flare onset, as observed in AIA hot lines like 131 and 94 Å (Figure 1 and its on-line animation, also Figure 3). According to GOES SXR 1-8 Å and AIA EUV 94 Å fluxes given in Figure 1(a), the flare starts at 17:20 UT. Both SXR and EUV light curves shows a well-defined precursor phase. The precursor phase terminates with the sudden X-ray or EUV emission enhancement at \sim 17:20 UT. In Figure 1(a), the time profile of 10830 Å exhibits an impulsive nature, even during the precursor phase. Before and during the precursor phase, there were several small-scale activities, shown as EUV brightenings, in the central region of the sigmoidal structure. The small-scale activities were accompanied by repetitive appearance and disappearance of prototype of a sigmoid MFR as reported by Cheng et al. (2015).

After a series of EUV brightenings, an unstable sigmoidal flux rope began to form at \sim 16:46 UT. After this moment, the sigmoidal threads get rapidly heated to the temperature visible in the AIA 131 Å passband (\sim 10 MK). Figure 1(b) gives a sample AIA 131 Å image taken at 16:55:59 UT, showing a snapshot of the formation process of the unstable sigmoid MFR, while panels (c) and (d) give the simultaneous information taken at He I 10830 Å and AIA 171 Å. Panel (e) gives a vector magnetogram taken by HMI. Around this moment, the sigmoid MFR became extremely unstable and quite ready for eruption. We can see a V-shaped brightening at 131 Å as well as 94 Å (see also Figure 3), which is most likely the signature of magnetic reconnection. The V-shaped brightening became round-shaped and was finally straightened during the slow rising.

The He I 10830 Å image in panel (c) has a smaller field of view, corresponding to the red boxed area in Figure 1(b). The most notable feature on the image is a filament connecting the targeted satellite sunspot to the penumbra region of the main sunspot in the active region. We can see that the 10830 Å filament is co-spatial with part of the hot channel. The V-shaped brightening, or the reconnection site is just located at the filament's end connecting the satellite sunspot. In Figure 2, we use time-space diagrams to show the brightening in hot temperature (AIA 131 Å), low temperature (AIA 171 Å) and He I 10830 Å during the precursor phase. The activation of the hot channel and 10830 Å filament can be seen in the time-space diagrams. When the erupting MFR was slowly rising, the filament with strong absorption got weakened and a partial eruption followed as seen from the on-line animation of Figure 1.

Figure 3 shows a sequence of images taken at AIA 94 Å before (panels (a)–(c)) and after the flare onset (panels (d)–(f)). Panel (a) is an AIA 94 Å image taken at 15:04 UT, showing

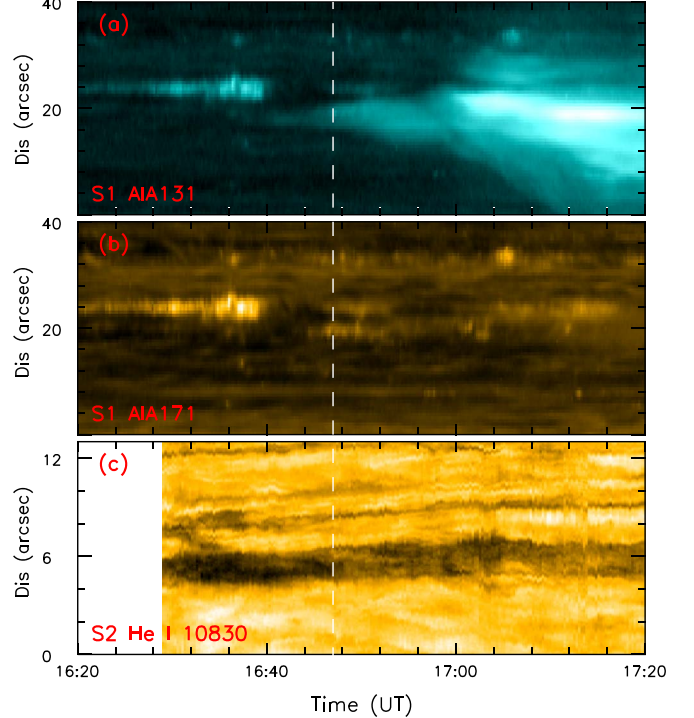


Figure 2. Space-time diagrams obtained with 131 and 171 Å images along the slice S1 in Figure 1 (b) and 10830 Å images along the slice S2 in Figure 1 (c). The dashed line indicates the starting time of the precursor phase (\sim 16:46 UT).

two groups of J-shaped MFRs, J1 and J2, and the overlying sheared arcade located between the green dotted lines in the field of view. Starting at about 15:09 UT, the overlying arcade became reconnected to the J-shaped flux rope J2, gradually forming a reverse S-shaped flux rope. The reconnection site, i.e., the middle part of the singular flux rope, was accompanied with EUV brightening even at 131 Å (Figure 2). The flux rope in panel (b) turned out to be an ephemeral appearance, it faded away after a few minutes. However, at \sim 16:46 UT, the magnetic reconnection between the overlying sheared arcade and the right J-shaped flux rope J2 occurred again, forming a V-shaped structure around the same reconnection site, as indicated in panel (c), it soon became flatten during the slow rising period. Meanwhile, a new unstable flux rope was quickly formed and expelled. Nevertheless, the original J-shaped MFR on the left side, J1, was still being there. It remained unaffected even when the flaring process was declining.

By comparing the maps of vertical magnetic field before and after the flare, we see an obvious fading of both positive and negative magnetic fluxes (Figure 4). It shows that significant magnetic cancellation has occurred during the flare. Contours overlaid on Figure 4 are photospheric vertical electric currents (VECs) of both signs obtained from HMI vector magnetograms with Ampere's law. The derivatives are approximated by a four-point differencing method, i.e., current density in each

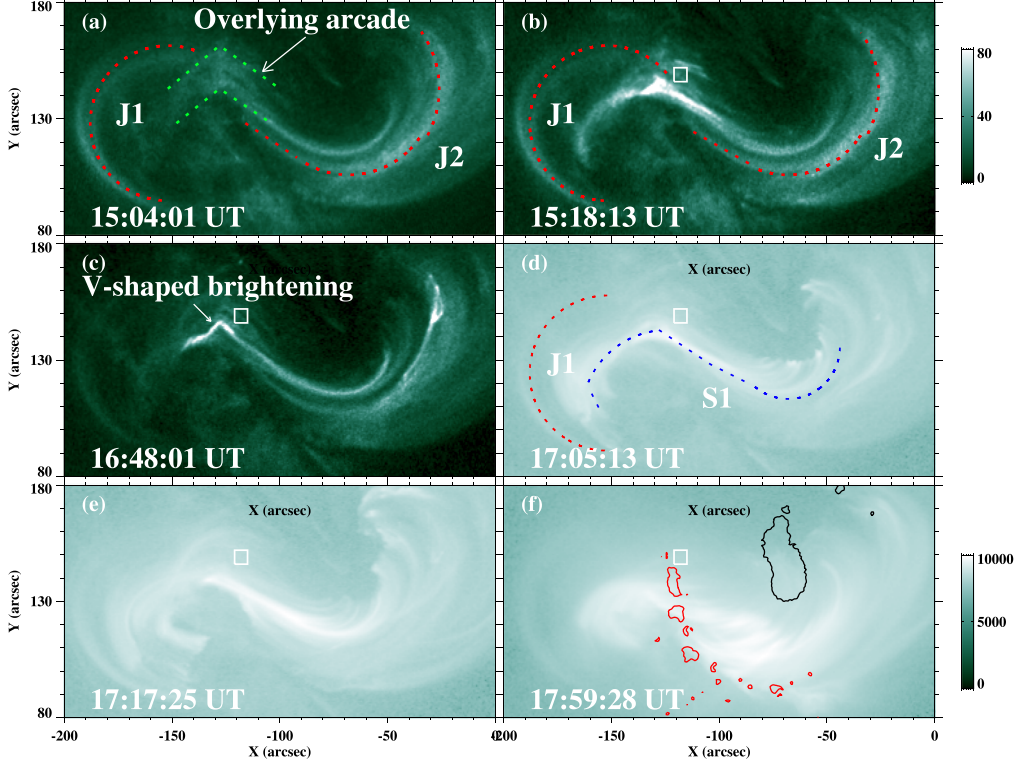


Figure 3. Snapshots for the formation and eruption of the hot channel taken at AIA 94 Å for the flare event. The red and blue dotted lines in panels delineate the two J-shaped magnetic arches (J1 and J2) and a formed sigmoid magnetic flux rope (S1). The overlying sheared arcade is between the green dotted lines in panel (a). In order to show J1 flux rope during the flaring period, images in panels (d)–(f) are displayed in logarithmic scale. Panel (f) is overlaid with contours of vertical magnetic field with the values of 2000 (black) and -1000 G (red). The white boxes in panels are the same as the smaller white box in Figure 1(d). The unit for the right color bars is $\text{DN pixel}^{-1} \text{ s}^{-1}$.

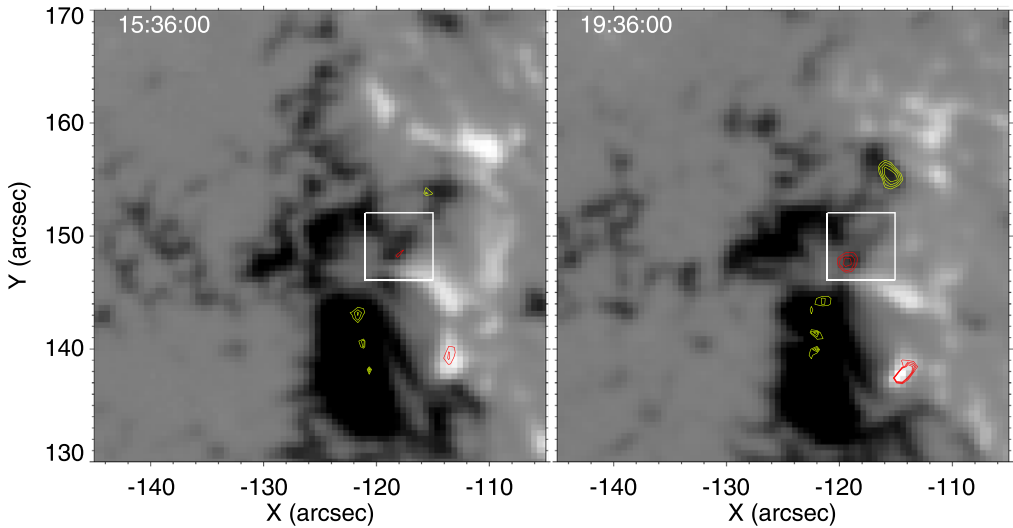


Figure 4. A comparison of vertical magnetic field and electric current before and after the flare. Backgrounds: vertical magnetic field with white (positive) and black (negative) saturating at ± 1000 G. Contours: photospheric vertical electric current (VEC) with the contour levels of $\pm 30, 35, 40, 45 \text{ mA m}^{-2}$ (blue: positive, red: negative). The two white boxes in the two panels are the same as the smaller box in Figure 1(d) and the boxes in Figure 3.

pixel is obtained by differencing corresponding set of four neighboring intersection pixels. For HMI, it has a noise level of ≈ 10 and ≈ 100 G for the longitudinal and transverse magnetic field, respectively (Schou et al. 2012; Tadesse et al. 2013). Taking its spatial resolution of 1.2 arcsec, we estimate the noise level of detecting VEC to be about 10 mA m^{-2} , which we can take as 1-sigma value. Based on the 3σ principle, Figure 4 shows the distribution of VEC with the contour levels of $\pm 30.0, 35.0, 40.0, 45.0 \text{ mA m}^{-2}$. We see that the magnitude of VEC of both signs has obviously increased in a number of places. We pay a special attention to the boxed area in Figure 4 where there is an obvious increase for the current, since the site is located at the footpoint area of the above-mentioned overlying magnetic loops. We plot the same boxes in the same places in all panels of Figure 3 to show the importance of the site. To find the relationship with the flare, we get six kinds of time profiles for the total VEC counted in the small box, taking six threshold values as the lower limit of integration. Six time profiles were obtained by integrating the values of the pixels in the boxed area with current density larger than $10.0, 15.0, 20.0, 25.0, 30.0$ and 35.0 mA m^{-2} respectively. It can be seen that all time profiles start to increase after $\sim 14:00$, much earlier than the starting time of the precursor phase ($\sim 16:46$ UT). However, the increase of VECs with larger current density lags behind. The VECs with density larger than 25 mA m^{-2} begin to increase at $\sim 15:00$. For these VECs, significant increase occurs simultaneously with the starting time of the precursor phase. Note that, before the starting time of the precursor phase, VECs with current density larger than 35.0 mA m^{-2} are barely above zero level.

Selecting a larger FOV for counting the current gives the similar results. Being shown in Figure 6 are the time profiles of VEC, vertical magnetic fluxes and mean horizontal magnetic field computed in a much bigger boxed area (Figure 1(d)). The bigger boxed area reaches the boundary of the main sunspot's penumbra. Panel (a) shows the temporal evolution of VEC counted from the pixels with the current density (unsigned) larger than 3.5 mA m^{-2} . The behavior of negative VEC agrees well with the time profiles 5–6 in Figure 5, except for the increase magnitude. The behavior of positive VEC is basically in agreement with the negative, except that there is small increase that peaks at $\sim 12:30$ UT. At the same time, we also obtained the evolution of vertical magnetic field (B_z) for the same region. The unsigned net magnetic fluxes of both signs are persistently declining, which confirms the picture given in Figure 4. In the end, the lowest panel of Figure 6 shows that there is an enhancement of horizontal magnetic field, and enhancement occurs after the flare's starting time at 17:20 UT.

Figure 7 shows a series of He I 10830 frames taken at different times during the precursor and flaring phase. With the GST's unprecedented high resolution, we see a very narrow bright line begin to appear at $\sim 16:57$ UT (Figure 7(a)). Later the narrow brightening line gets weakened and evolves into a

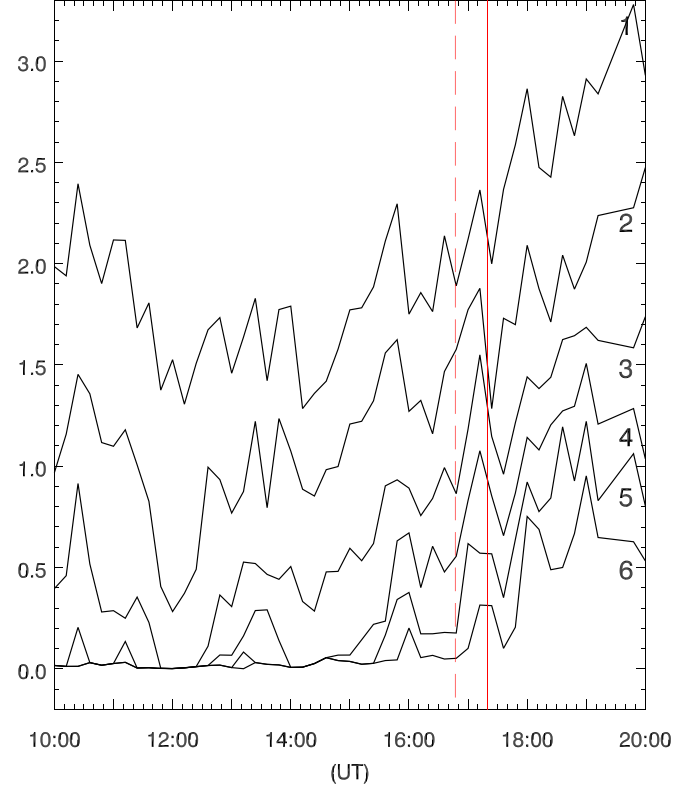


Figure 5. Curves 1–6 give the time profiles of total VEC integrated in the boxed area in Figure 4 from the pixels with current density larger than $10.0, 15.0, 20.0, 25.0, 30.0$, and 35.0 mA m^{-2} respectively. The dashed and solid lines indicate the starting times of the precursor phase ($\sim 16:46$ UT) and the flare's onset time ($\sim 17:20$ UT).

bright patch with a narrow dark (or absorption) front. Note that the narrow dark front moves along with the erupting hot channel and has no associated EUV brightening front can be found (see on-line animation of Figure 1). The width of the dark front is about 300–400 km, so it is quite similar to the ultra-narrow negative flare front reported by Xu et al. (2016). During the eruption of the hot channels, we see changes of brightness and structural changes in the 10830 Å filament. However, the filament survived the eruption, giving a picture of partial eruption.

4. Discussions and Summary

In this event, for the two J-shaped hot channels which form the sigmoidal structure in the active region, they did not reconnect with each other to erupt. Instead, one J-shaped hot channel reconnects with the overlying sheared arches that run striding the sigmoid in the midway. This kind of magnetic reconnection can be referred as the third-party joining in magnetic reconnection. For this event, the magnetic reconnection between the two hot channels is observed as a localized

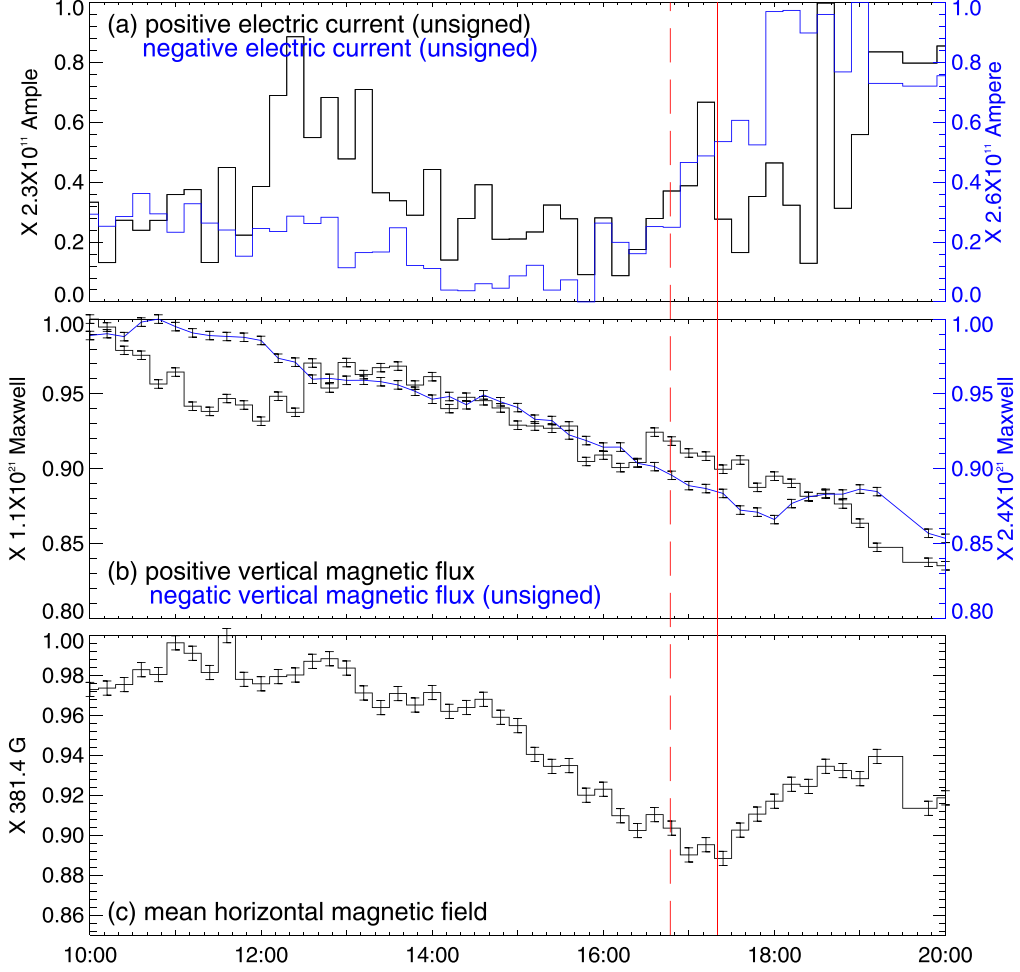


Figure 6. A series of normalized time profiles for VEC and magnetic field in the bigger white-boxed area of Figure 1(d). Tagging given in each panel gives the meaning of corresponding time profile. The total VECs of both signs were integrated from the pixels with the absolute current density larger than 35.0 mA m^{-2} . The plotted error bar correspond to 1 standard deviation calculated with corresponding de-trended time profile. The dashed and solid lines indicate the starting times of the precursor phase ($\sim 16:46 \text{ UT}$) and the flare's onset time ($\sim 17:20 \text{ UT}$).

V-shaped EUV brightening or heating. Through the instantaneous reconnection, they form an erupting flux rope. We further find that another original J-shaped hot channel remains in existence even after the end of the flare.

In the solar corona, the plasma β value is $\ll 1$, so coronal magnetic field is basically force-free. Extrapolation is often implemented to derive coronal magnetic structure using the photospheric vector magnetic field as the boundary conditions. In this work, we have adopted the marginally unstable model of AR 12158 presented by Liu et al. (2018). This model is constructed based on the line-of-sight photospheric magnetogram observed by HMI before the flare using the flux rope insertion method developed by van Ballegooijen (2004). This method has been successfully applied to study sigmoid active regions (e.g., Savcheva & van Ballegooijen 2009; Su 2019 references therein). A comparison of AIA observations and

selected field lines from the marginally unstable model is shown in Figure 8. We find that the two J-shaped sheared arcades and the overlying arcade from the model are qualitatively in good agreement with the AIA observations in 94 Å. The picture is generally in agreement with the tether-cutting model (Moore et al. 2001), but with some differences. We usually believe that two groups of highly sheared J-shaped magnetic arches turn into an upward erupting flux rope via magnetic reconnection. In this way, the pre-eruption magnetic configuration is assumed to erupt as a whole, i.e., the entire sigmoid magnetic arches should be erupted and thus disappeared. A scrutiny to the figures in earlier literatures actually shows that, in some cases, only one J-shaped magnetic arch was erupted, leaving another J-shaped magnetic arch totally unaffected (e.g., Sterling et al. 2000; Moore et al. 2001). However, the picture is different from the meaning of partial

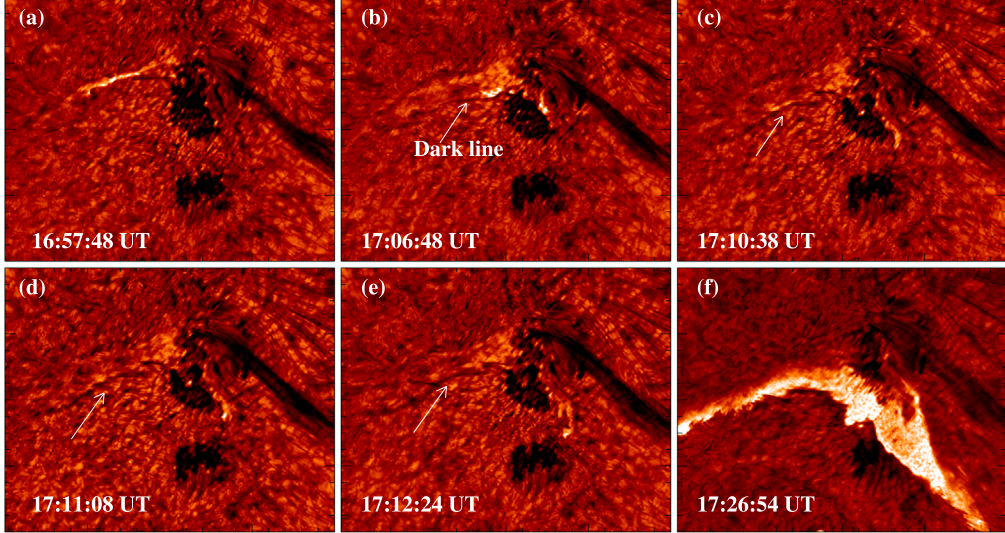


Figure 7. High resolution He I 10830 Å frames taken at different times during the precursor phase (panels (a)–(e)) and the moment of flaring (panel (f)). The white arrows point to the narrow dark front during the precursor phase (also see on line animation of Figure 1).

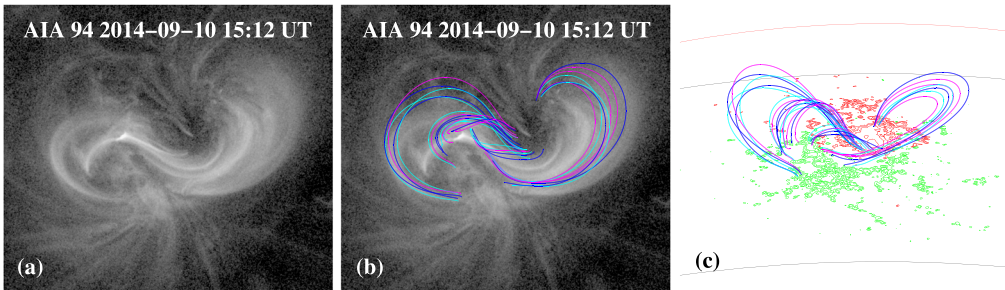


Figure 8. AIA images in 94 at 15:12 UT is displayed in (a) and (b) as background. Panels (b) and (c) give the modeled extrapolation for the two groups of magnetic arches and the overlying magnetic arcade before onset of the flare.

eruptions. In a partial eruption, the magnetic flux embedded filament may split into an erupting part and a remaining part (Liu et al. 2012; Chen et al. 2018; Cheng et al. 2018). For the case in which only half of a sigmoidal magnetic structure is erupted, it is the partial eruption of a new kind. We can term the partial eruption of sigmoidal hot channels like the one in this event as a half eruption.

In this paper, one important finding is that, with the starting time of the precursor phase, strong VECs appeared at the footpoint region of the overlying magnetic arcade. Strong electric current is defined in such a way that its density is three times larger the noise level ($\sim 10 \text{ mA m}^{-2}$) estimated from uncertainties in measuring transverse magnetic field. Combining the error estimation given by Sharykin et al. (2020), we take the noise level as the standard deviation (1σ) of VECs in this paper. To be on the safe side, all the points in the VEC time profiles 5–6 in Figure 5 and the VEC time profiles in Figure 6(a) are from signals of 3σ significance. The time

profiles 5–6 in Figure 5 show that strong electric current enhanced simultaneously with the starting time of the precursor phase. It is worth noting that, before the precursor phase, strong electric current with its density larger than 35 mA m^{-2} is actually around zero. It seems that the enhanced electric current may have flowed into the MFR, and plays a vital role in powering the eruption. The powering process may have played a triggering role for the magnetic reconnection between the two hot channels. We also note that, the VECs with lower current density begin to increase much earlier than the precursor phase. The increase may be responsible for the several earlier brightenings mentioned above.

The time profiles in Figure 6(a) for strong VEC in a much larger FOV centered at the footpoint region show similar behaviors, especially for the negative current (the same sign as the localized enhanced current in the footpoint region). Also, the magnetic fluxes of positive and negative signs (vertical magnetic field) in the larger area around the reconnection site

are persistently declining, which indicates ongoing magnetic cancellation. It is quite different from the picture of energy build-up or current-carrying flux emergence (Leka et al. 1996; Toriumi & Wang 2019), which shows increase for the vertical current and magnetic flux in the active regions. From our observations, it further shows that magnetic activities actually occur in a much broader area and happen all the time.

Meanwhile, the horizontal magnetic field is enhanced in the flare region after the onset time of the flare's impulsive phase. This kind of flare-related variation of horizontal magnetic field has been reported by many authors and is explained as the result of magnetic reconnection or re-configuration like contraction of magnetic field after flares (Ji et al. 2007; Joshi et al. 2009; Wang & Liu 2010; Simões et al. 2013).

In this event, Cheng et al. (2015) have reported a non-thermal component from IRIS spectral observations during the formation of the erupting flux rope. We find a narrow He I 10830 Å absorption front along the erupting hot channel. The absorption front moves with the erupting hot channel. Because the narrow dark absorption front in He I 10830 Å, similar to the one reported by Xu et al. (2016), has no counterpart EUV bright front, we can regard it to be produced by collisions of non-thermal electrons (Ding et al. 2005). Furthermore, the 10830 Å light curve in Figure 1(a) exhibits an impulsive nature. They provide solid evidences supporting that particle acceleration occurs during the flare's precursor phase. While the presence of the dark front confirms earlier findings for the existence of nonthermal electrons in precursor phases, it serves to answer the question of how the nonthermal electrons are produced. It shows that the interaction between the erupted hot channel and the overlying or surrounding magnetic field may have yielded particle acceleration, because there is no sign for the existence of a vertical current sheet.

In summary, using high resolution multi-wavelength observations, we give a detailed analysis to the precursor phase of the X1.6-class flare on 2014 September 10. Main results reported in this paper can be listed as the following:

1. We have observed and defined a kind of half eruption for sigmoidal magnetic structures. During the half eruption, magnetic reconnection occurs between one J-shaped MFR and the overlying sheared magnetic arcade. The magnetic reconnection still forms an unstable MFR that finally gets erupted as the flare, leaving another J-shaped MFR untouched.
2. With vector magnetograms from SDO/HMI, we are able to pick-out the precursor-associated enhancement of the strong photospheric vertical electric currents. In this paper, electric current is defined as strong when its current density is over $\sim 30 \text{ mA m}^{-2}$, which equals to 3σ value. The enhancement of the strong electric current around the footpoint region of the overlying arcade may

have powered the magnetic reconnection mentioned above.

3. The interaction between the erupted hot channel and the overlying or surrounding magnetic field has yielded particle acceleration.

Acknowledgments

We are grateful for the anonymous referee who has helped to improve the paper. SDO data were made available by the NASA/SDO AIA and HMI science teams. We thank the teams for providing the data. This work was supported by the National Natural Science Foundation of China under grants 11773061 and 11790302. This work was also supported by the West Young Scholars Programs CAS grant No. 2017XBQNXZ-A-007. We thank Nanjing University, Key Lab Modern Astronomy and Astrophysics, No. KLSA 202106 of CAS Key Lab of Solar Activity, NAOC, Key Lab for DMSA, CAS for their support and High-level Flexible Talent Program of Xinjiang Uygur Autonomous Region. BBSO operation is supported by NJIT and US NSF AGS-1821294 grant. GST operation is partly supported by the Korea Astronomy and Space Science Institute, the Seoul National University, and the Key Laboratory of Solar Activities of Chinese Academy of Sciences (CAS) and the Operation, Maintenance and Upgrading Fund of CAS for Astronomical Telescopes and Facility Instruments.

References

Asai, A., Nakajima, H., Shimojo, M., et al. 2006, *PASJ*, **58**, L1
 Aurass, H., Vršnak, B., Hofmann, A., & Rudžjak, V. 1999, *SoPh*, **190**, 267
 Awasthi, A. K., Liu, R., Wang, H., Wang, Y., & Shen, C. 2018, *ApJ*, **857**, 124
 Bamba, Y., Lee, K.-S., Imada, S., & Kusano, K. 2017, *ApJ*, **840**, 116
 Bumba, V., & Křivský, L. 1959, *Bull. Astron. Inst. Czech.*, **10**, 221
 Canfield, R. C., Hudson, H. S., & McKenzie, D. E. 1999, *Geophys. Res. Lett.*, **26**, 627
 Cao, W., Gorceix, N., Coulter, R., et al. 2010, *AN*, **331**, 636
 Chen, H., Duan, Y., Yang, J., Yang, B., & Dai, J. 2018, *ApJ*, **869**, 78
 Chen, X., Yan, Y., Tan, B., et al. 2019, *ApJ*, **878**, 78
 Cheng, X., Ding, M. D., & Fang, C. 2015, *ApJ*, **804**, 82
 Cheng, X., Ding, M. D., Zhang, J., et al. 2014, *ApJL*, **789**, L35
 Cheng, X., Kliem, B., & Ding, M. D. 2018, *ApJ*, **856**, 48
 Cheng, X., Zhang, J., Liu, Y., & Ding, M. D. 2011, *ApJL*, **732**, L25
 Chifor, C., Mason, H. E., Tripathi, D., Isobe, H., & Asai, A. 2006, *A&A*, **458**, 965
 Chifor, C., Tripathi, D., Mason, H. E., & Dennis, B. R. 2007, *A&A*, **472**, 967
 Ding, M. D., Li, H., & Fang, C. 2005, *A&A*, **432**, 699
 Dudík, J., Polito, V., Janvier, M., et al. 2016, *ApJ*, **823**, 41
 Fárník, F., Hudson, H. S., Karlický, M., & Kosugi, T. 2003, *A&A*, **399**, 1159
 Fletcher, L., Dennis, B. R., Hudson, H. S., et al. 2011, *SSRv*, **159**, 19
 Goode, P. R., Coulter, R., Gorceix, N., Yurchyshyn, V., & Cao, W. 2010, *AN*, **331**, 620
 Graham, D. R., & Cauzzi, G. 2015, *ApJL*, **807**, L22
 Harrison, R. A., Waggett, P. W., Bentley, R. D., et al. 1985, *SoPh*, **97**, 387
 Hernandez-Perez, A., Su, Y., Veronig, A. M., et al. 2019, *ApJ*, **874**, 122
 Holman, G. D., Sui, L., Schwartz, R. A., & Emslie, A. G. 2003, *ApJL*, **595**, L97
 James, A. W., Green, L. M., Palmerio, E., et al. 2017, *SoPh*, **292**, 71
 Ji, H., Huang, G., & Wang, H. 2007, *ApJ*, **660**, 893
 Joshi, B., Veronig, A., Cho, K. S., et al. 2009, *ApJ*, **706**, 1438

Kashapova, L. K., Meshalkina, N. S., & Kisil, M. S. 2012, *SoPh*, **280**, 525

Leka, K. D., Canfield, R. C., McClymont, A. N., & van Driel-Gesztelyi, L. 1996, *ApJ*, **462**, 547

Lemen, J. R., Title, A. M., Akin, D. J., et al. 2012, *SoPh*, **275**, 17

Li, D., Li, Y., Su, W., Huang, Y., & Ning, Z. 2018, *ApJ*, **854**, 26

Li, D., Ning, Z. J., & Zhang, Q. M. 2015, *ApJ*, **813**, 59

Li, T., & Zhang, J. 2015, *ApJL*, **804**, L8

Liu, R., Kliem, B., Török, T., et al. 2012, *ApJ*, **756**, 59

Liu, T., Su, Y., Cheng, X., van Ballegooijen, A., & Ji, H. 2018, *ApJ*, **868**, 59

Metcalf, T. R., Canfield, R. C., Hudson, H. S., et al. 1994, *ApJ*, **428**, 860

Moore, R. L., Hagyard, M. J., & Davis, J. M. 1987, *SoPh*, **113**, 347

Moore, R. L., Sterling, A. C., Hudson, H. S., & Lemen, J. R. 2001, *ApJ*, **552**, 833

Patsourakos, S., Vourlidas, A., & Stenborg, G. 2013, *ApJ*, **764**, 125

Pesnell, W. D., Thompson, B. J., & Chamberlin, P. C. 2012, *SoPh*, **275**, 3

Priest, E., & Forbes, T. 2000, Magnetic Reconnection: MHD Theory and Applications (Cambridge: Cambridge Univ. Press)

Rust, D. M., & Kumar, A. 1996, *ApJL*, **464**, L199

Savcheva, A., & van Ballegooijen, A. 2009, *ApJ*, **703**, 1766

Scherrer, P. H., Schou, J., Bush, R. I., et al. 2012, *SoPh*, **275**, 207

Schou, J., Scherrer, P. H., Bush, R. I., et al. 2012, *SoPh*, **275**, 229

Schrijver, C. J. 2009, *AdSpR*, **43**, 739

Sharykin, I. N., Zimovets, I. V., & Myshyakov, I. I. 2020, *ApJ*, **893**, 159

Shen, J., Wang, Y., Zhou, T., & Ji, H. 2017, *ApJ*, **835**, 43

Simões, P. J. A., Fletcher, L., Hudson, H. S., & Russell, A. J. B. 2013, *ApJ*, **777**, 152

Sterling, A. C., Chifor, C., Mason, H. E., Moore, R. L., & Young, P. R. 2010, *A&A*, **521**, A49

Sterling, A. C., Hudson, H. S., Thompson, B. J., & Zarro, D. M. 2000, *ApJ*, **532**, 628

Su, Y.-n 2019, *ChJAA*, **43**, 305

Sun, X. 2013, arXiv:1309.2392

Tadesse, T., Wiegmann, T., Inhester, B., et al. 2013, *A&A*, **550**, A14

Tan, B., Yu, Z., Huang, J., Tan, C., & Zhang, Y. 2016, *ApJ*, **833**, 206

Tappin, S. J. 1991, *A&AS*, **87**, 277

Tian, H., Young, P. R., Reeves, K. K., et al. 2015, *ApJ*, **811**, 139

Toriumi, S., & Wang, H. 2019, *LRSP*, **16**, 3

van Ballegooijen, A. A. 2004, *ApJ*, **612**, 519

Wang, H., & Liu, C. 2010, *ApJL*, **716**, L195

Wang, H., Liu, C., Ahn, K., et al. 2017, *NatAs*, **1**, 0085

Wang, Y., Su, Y., Shen, J., et al. 2018, *ApJ*, **859**, 148

Warren, H. P., & Marshall, A. D. 2001, *ApJL*, **560**, L87

Wöger, F., & von der Lühe, O. 2007, *ApOpt*, **46**, 8015

Xu, Y., Cao, W., Ding, M., et al. 2016, *ApJ*, **819**, 89

Zhang, J., Cheng, X., & Ding, M.-D. 2012, *NatCo*, **3**, 747

Zhang, Q. M., Su, Y. N., & Ji, H. S. 2017, *A&A*, **598**, A3

Zhang, Y., Tan, B., Karlický, M., et al. 2015, *ApJ*, **799**, 30

Zhao, J., Gilchrist, S. A., Aulanier, G., et al. 2016, *ApJ*, **823**, 62

Zhou, G. P., Zhang, J., & Wang, J. X. 2016, *ApJL*, **823**, L19